

Leveraging Secondary Storage to Simulate Deep 54-qubit Sycamore Circuits

Edwin Pednault^{*1}, John A. Gunnels¹, Giacomo Nannicini¹, Lior Horesh¹, and Robert Wisnieff¹

¹IBM T.J. Watson Research Center, Yorktown Heights, NY

Abstract

In a recent paper, we showed that secondary storage can extend the range of quantum circuits that can be practically simulated with classical algorithms. Here we refine those techniques and apply them to the simulation of Sycamore circuits with 53 and 54 qubits, with the entanglement pattern ABCDCDAB that has proven difficult to classically simulate with other approaches. Our analysis shows that on the Summit supercomputer at Oak Ridge National Laboratories, such circuits can be simulated with high fidelity to arbitrary depth in a matter of days, outputting all the amplitudes.

1 Introduction

There has been tremendous progress in the construction of quantum computers with superconducting qubits [4]. As the hardware progresses, it is increasingly difficult to classically simulate the circuits that can be executed on existing chips, a crucial task to – among other things – verify that the degree to which hardware is behaving as expected. The literature contains several papers that discuss this task and that have been published or posted online in the last two years [14, 3, 7, 10, 5, 11, 16, 6, 17, 8, 18]. Here we extend the analysis on the use of secondary storage initially reported in our previous work [14]. As we argued in that paper, secondary storage can extend the computational reach of supercomputers for the simulation of quantum circuits — an idea initially suggested by [9]. We estimate that on the Summit supercomputer at Oak Ridge National Laboratories, secondary storage allows the simulation of 53- and 54-qubit Sycamore circuits [15] with high fidelity to arbitrary depth. The Sycamore circuits are a direct descendant of the “universal random circuits” described in [2]. In particular, for 20 cycles of the entanglement pattern ABCDCDAB, which is specifically designed to challenge classical simulation algorithms, we estimate that the calculations would take approximately two and a half days. While we did not carry out these calculations, we provide a detailed description of the proposed simulation strategy as well as the time estimation methodology, which is based on published results and on internal benchmarks. The main building blocks of our approach are the same as those that we discussed in [14], namely: exploitation of separable gates via a hyperedge representation of the tensor network; allowing contractions between non-adjacent tensors; tensor slicing; and sporadic read/write operations to access/store slices of the quantum state in secondary storage.

The rest of this paper is organized as follows. In Sect. 2 we provide a review of the main building blocks of our simulation strategy. Sect. 3 describes the class of circuits studied in this work. Sect. 4 gives a detailed explanation of the simulation strategy and its use of secondary storage. Sect. 5 concludes the paper by estimating the time required by the proposed simulations, and discussing the methodology to compute such estimates.

^{*}Corresponding author; pednault@us.ibm.com

2 Brief overview of tensor contraction deferral

The simulation algorithm that we propose is based on the idea of partitioning a quantum circuit into subcircuits that can be simulated independently, at the expense of extra bookkeeping to account for entanglement between subcircuits. We ensure that the final results are correct by appropriately recombining the different subcircuits and, in some sense, “resolving” the entanglement. Rather than insisting that all subcircuits reside in primary storage, i.e., RAM, we allow for storing the results of some of the calculations on secondary storage, i.e., disk. This is particularly effective when combined with slicing techniques, which further partition the quantum state by iteratively fixing the value of some of the indices in the tensor network.

We now give a brief overview of the main components of our simulation strategies; for details and several examples, we refer the reader to our earlier work [14]. A *tensor* is a multilinear map with a set of indices to address its elements. In the context of this paper, each index takes value in $\{0, 1\}$. As discussed in [14], a *tensor network* is a hypergraph $G = (V, E)$ such that each node is associated with a tensor and each hyperedge with an index of the adjacent tensors. Hyperedges between nodes represent shared indices that must be summed over. A summation over shared indices is called a *contraction*. A tensor $A_{i_1, \dots, i_m, j_1, \dots, j_m}$ is *diagonal* if it is nonzero only if $i_k = j_k$ for $k = 1, \dots, m$. A tensor is *separable* if it can be obtained from a diagonal tensor with a permutation, i.e., there exist functions f_1, \dots, f_m such that $A_{f_1(j_1, \dots, j_m), \dots, f_m(j_1, \dots, j_m), j_1, \dots, j_m}$ is diagonal. Our hypergraph representation is designed to take advantage of separable tensors, since the computational resources necessary to perform a contraction between several tensors can be significantly reduced in the presence of indices shared among multiple tensors — represented by hyperedges. Given a quantum circuit, we can construct a tensor network by letting the gates correspond to tensors, and the qubit lines roughly correspond to the indices (i.e. edges and hyperedges). To simulate large circuits, we rely extensively on *contraction deferral* and *tensor slicing*, which we describe more fully below.

Contraction deferral is a technique first introduced in [1]. Its use in large-scale simulations was pioneered in [14]. Contraction deferral is defined as the contraction of arbitrary sets of (potentially non-adjacent) tensors in the tensor network; this is in contrast with the adjacent contraction discussed in the seminal work [12] and in several subsequent papers, e.g., [3]. A deferred contraction performs the usual summation over shared indices (i.e., edges interior to the set being contracted), and applies an outer product to the non-shared indices. As it is a generalization of the traditional adjacent contraction, contraction deferral opens up new simulation strategies that can lead to reduced memory requirements. In particular, we partition the tensor network into sub-hypergraphs corresponding to subcircuits, each of which includes fewer qubits than the initial circuit. Within each circuit we perform computations following the “Schrödinger approach” [1], i.e., evolving the full quantum state of the subcircuit by applying layers of gates one at a time. To do so, we must use contraction deferral whenever we apply tensors corresponding to entangling gates between different subcircuits.

Tensor slicing is the idea of iterating over several instances of a circuit in which certain hyperedges (i.e., tensor indices) are fixed to one of their possible values. While this does not necessarily reduce the number of operations to be performed, it allows reordering the computations so that they take place in ways that are potentially more efficient. This is particularly crucial when using secondary storage, which is slower than is primary storage and must therefore be used sparingly; with tensor slicing, we reorganize the calculations so that only a few selected slices (rather than full tensors) reside in primary storage at any given time. Our scheme extends the simulation strategy in [9]: we choose a set of indices, slice them by looping over every possible combination of their values, and use a superset of those qubits to efficiently organize and address information located in secondary storage.

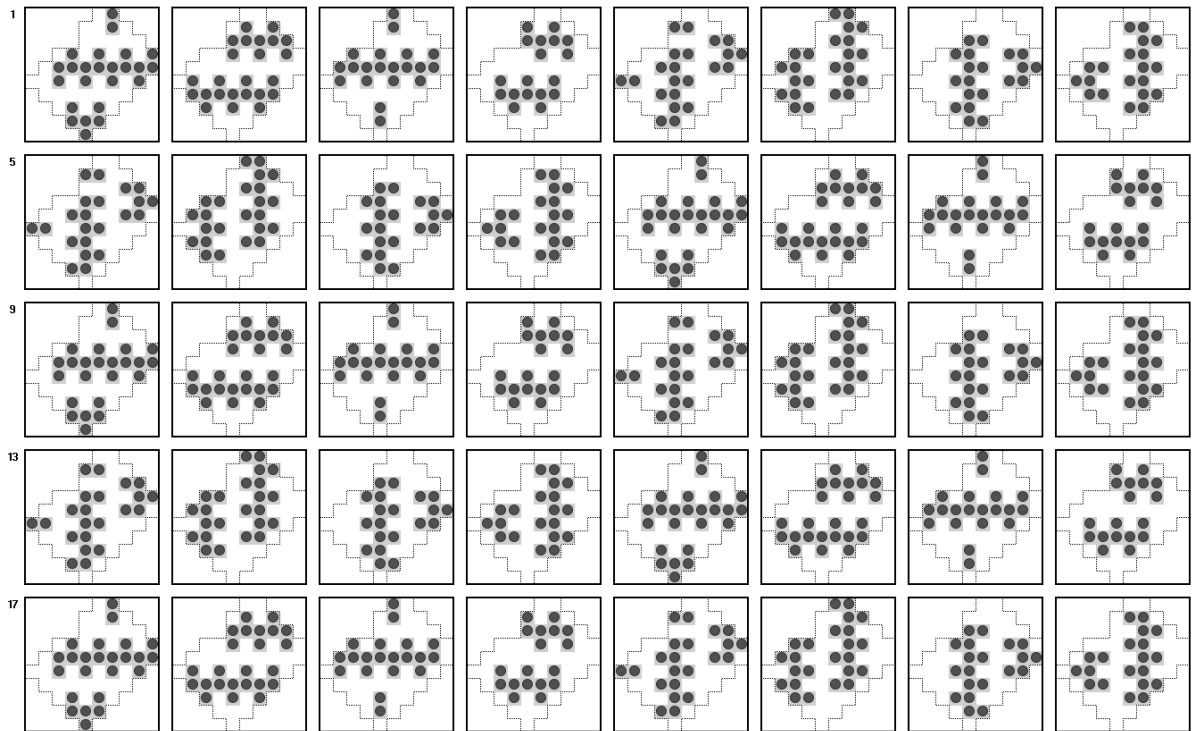


Figure 1: Gate pattern for a 20-cycle, 53-qubit, Sycamore ABCDCDAB circuit. Single-qubit gates are merged into their neighboring two-qubit gates, and the two-qubit gates in each cycle are partitioned into two layers for illustration purposes to make the individual gates easy to identify. These transformations result in the 40-layer circuit depicted. Dots and shading are used to identify which pairs of qubits are being operated upon.

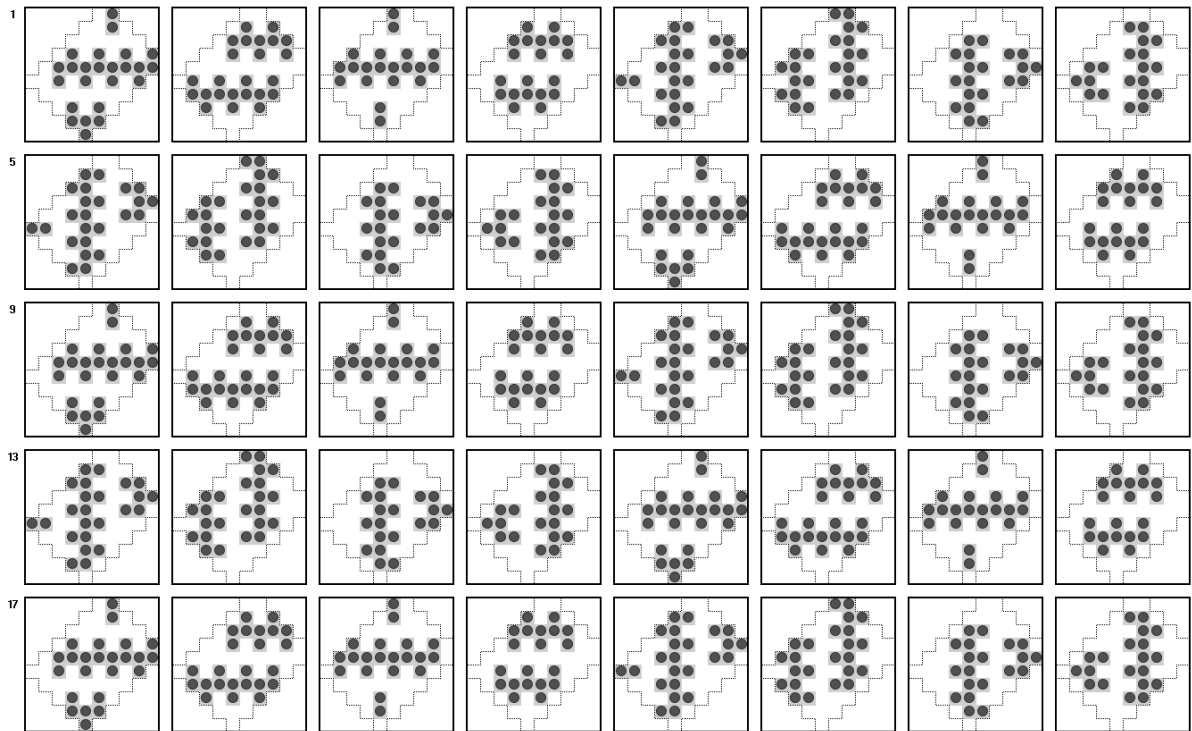


Figure 2: Gate pattern for a 20-cycle, 54-qubit, Sycamore ABCDCDAB circuit. Single-qubit gates are merged into their neighboring two-qubit gates, and the two-qubit gates in each cycle are partitioned into two layers for illustration purposes to make the individual gates easy to identify. These transformations result in the 40-layer circuit depicted. Dots and shading are used to identify which pairs of qubits are being operated upon.

3 Sycamore circuits

A recent paper [15] describes a new class of random quantum circuits consisting of alternating layers of single-qubit gates and two-qubit gates. The combination of a layer of single-qubit gates followed by a layer of two-qubit gates is referred to in [15] as a *cycle*. This paper discusses the classical simulation of circuits of this class; hence, we describe them here in more detail. Gates are applied to all qubits in each single-qubit gate layer, and to almost all qubits in each two-qubit gate layer. The two-qubit gates are all non-diagonal and their unitary representation varies as a function of both the location of the gate within the qubit layout, and the depth at which the gate is applied in the circuit. The former reflects variations in gate tuning, while the latter reflects variations in pulse synchronization over time. Circuits consist of several cycles of single-qubit gates followed by two-qubit gates, together with a final layer of single-qubit gates. The single-qubit gates are randomly selected from the set $\{\sqrt{X}, \sqrt{Y}, \sqrt{W}\}$. The two-qubit gates implement the following unitary:

$$\begin{bmatrix} 1 & 0 & 0 & 0 \\ 0 & e^{i(\Delta_+ + \Delta_-)} \cos \theta & -ie^{i(\Delta_+ - \Delta_{-, \text{off}})} \sin \theta & 0 \\ 0 & -ie^{i(\Delta_+ + \Delta_{-, \text{off}})} \sin \theta & e^{i(\Delta_+ - \Delta_-)} \cos \theta & 0 \\ 0 & 0 & 0 & e^{i(2\Delta_+ - \phi)} \end{bmatrix}, \quad (1)$$

where θ and ϕ are nominally 90° and 30° , respectively, and where Δ_+ , Δ_- , and $\Delta_{-, \text{off}}$ are detuning terms. For simulation purposes, all single-qubit gates can be aggregated with neighboring two-qubit gates, yielding an equivalent circuit consisting of (potentially unique) two-qubit gates only. The method for selecting single-qubit gates ensures that these two-qubit unitary operations are also randomized. The difficulty of simulation is therefore determined entirely by the pattern of two-qubit gates in the circuit.

Figs. 1 and 2 illustrate the “ABCDCDAB” patterns of two-qubit gates used in the 53- and 54-qubit random circuits described in [15] to test the Sycamore quantum device. This pattern is intentionally devised to make the resulting circuits difficult to simulate classically. For illustration purposes, each cycle of two-qubit gates is depicted as two layers in the figures, so that we can unambiguously indicate the pairs of qubits involved in each gate operation (i.e., vertical pairs versus horizontal pairs). Thus, the first two layers of two-qubit gates illustrated correspond to the “A” cycle, the next two layers to the “B” cycle, and so on. In this representation, the first row corresponds to an “ABCD” sequence of cycles, the second row corresponds to a “CDAB” sequence of cycles, and the five rows illustrated in Figs. 1 and 2 correspond to the 20-cycle circuits generated according to the ABCDCDAB rules described in [15].

4 Proposed simulation strategy

In [9] the authors suggest that solid-state disk, or more generally secondary storage, could be used to supplement main memory in order to simulate circuits whose quantum states are too large to store in main memory alone. In [14], we combined our in-memory methods with those of [9], describing a viable computation scheme that exploits secondary storage to simulate deeper circuits than was thought possible. We now apply the approach discussed in [14] to 53- and 54-qubit Sycamore circuits, showing in this section a computation scheme that allows their simulation on an existing supercomputer, Summit. The cost of such scheme is discussed in Sect. 5.

The simulation method in [9] can be seen as a tensor slicing approach. Qubits (and the corresponding tensor indices) are divided into “global” qubits, which are sliced and used to address across processing nodes, and “local” qubits, corresponding to tensor indices used to address tensor slices stored on each processing node. In [9], circuits are partitioned so that all gates within a subcircuit can be applied to the local slice of the quantum state, without communicating quantum state information among processing nodes. Such zero-communication updates of a local quantum state are possible when all non-diagonal

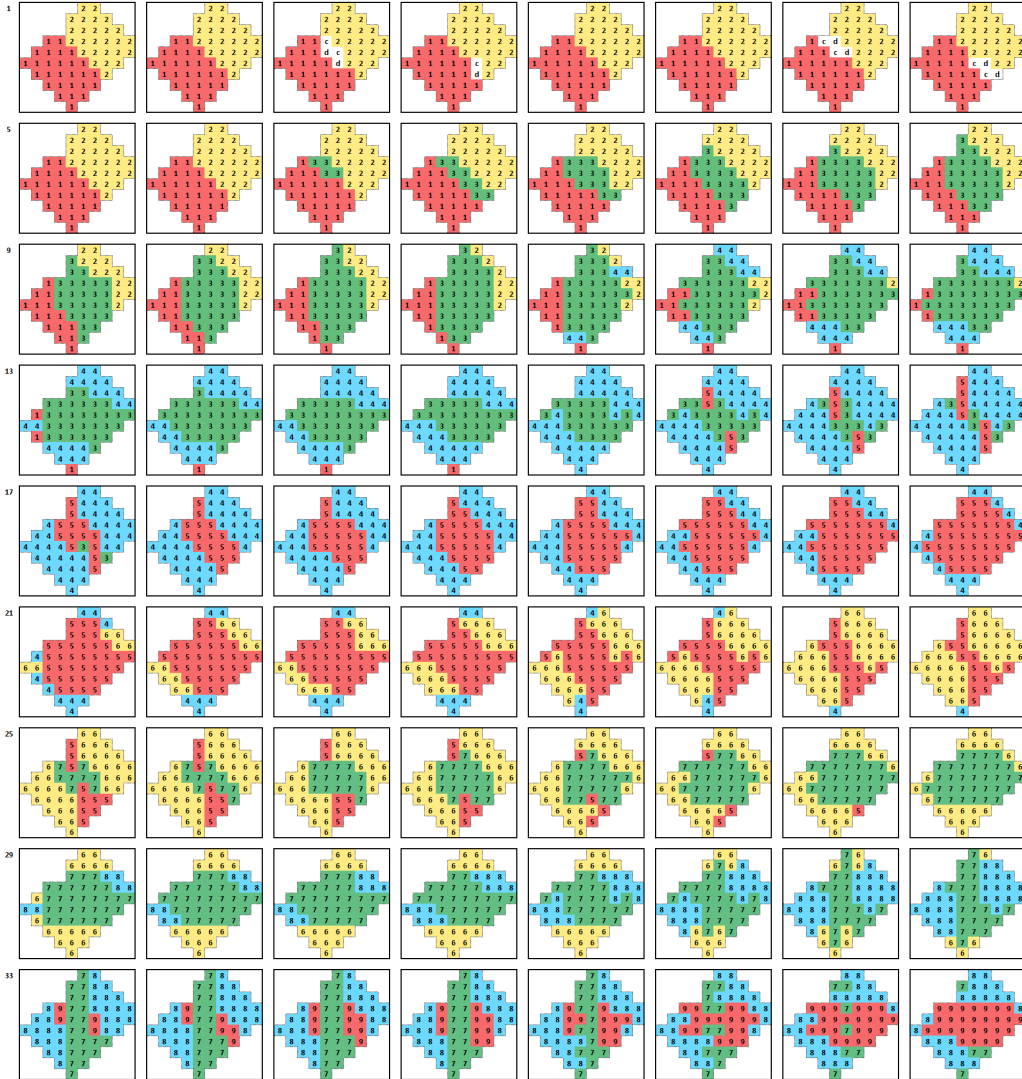


Figure 3: Partitioning of a 36-cycle, 53-qubit, Sycamore ABCDCDAB circuit to leverage secondary storage.

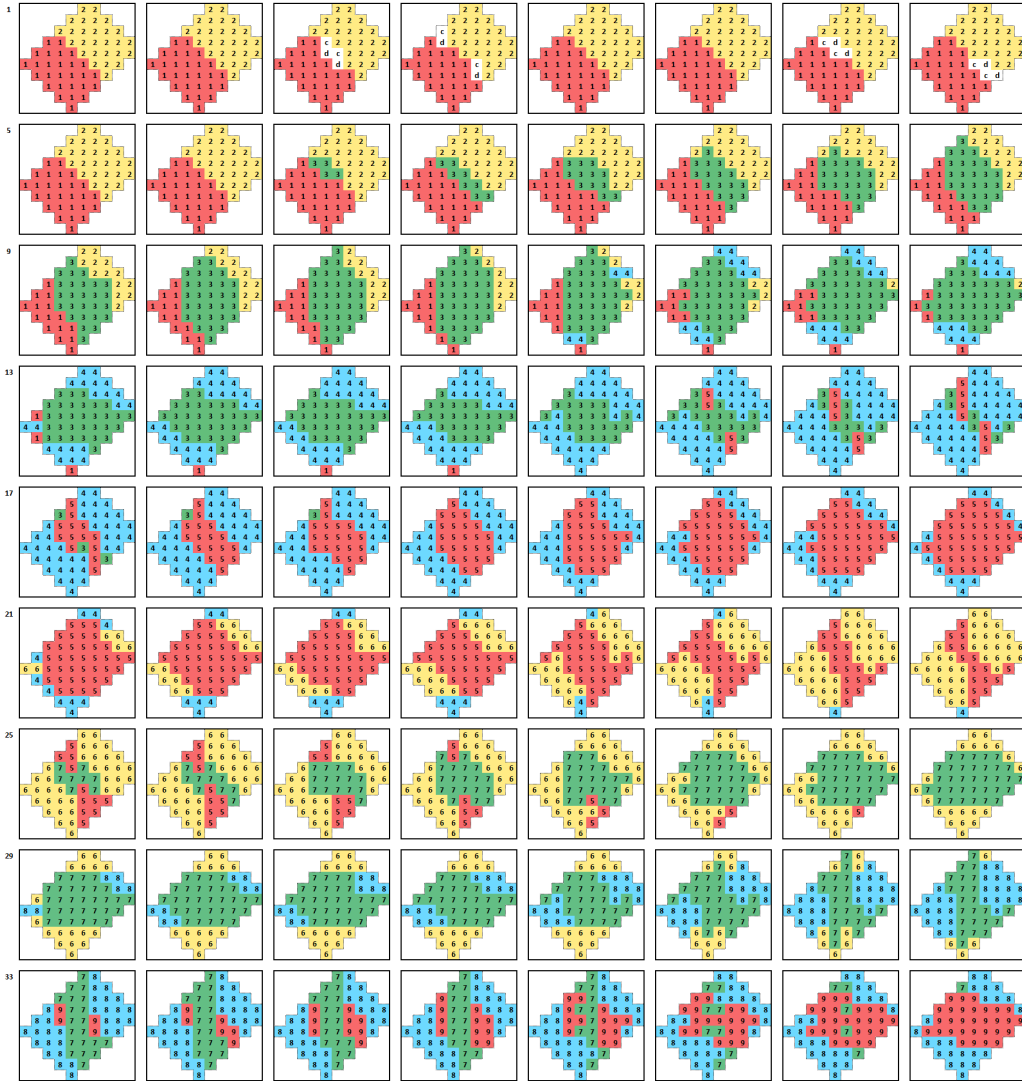


Figure 4: Partitioning of a 36-cycle, 54-qubit, Sycamore ABCDCDAB circuit to leverage secondary storage.

gates in a subcircuit are applied to local qubits only. They are also possible for a handful of additional circumstances described in [9]. In effect, circuits are partitioned by selecting different subsets of local qubits and analyzing which gates can be applied to them without communication. This determines the subcircuits. During simulation, communication between processing nodes occurs only when the simulation switches from one subcircuit to another. When a communication phase takes place, the memory layout of quantum state tensors is reorganized so that different global and local qubits (i.e., tensor indices) are selected, according to the subcircuits that have to be simulated in the subsequent phase.

The in-memory method that we presented in [14] considers circuit partitionings in which the resulting tensors either fit in available aggregate primary memory in their entirety, or their slices can be computed using available primary memory (using other tensors already computed and stored in primary memory). With this approach, the resulting tensors and/or their slices will generally be larger than the primary memories of individual processing nodes; this represents a difference between [14] and [9].

As discussed in [14], we combine the zero-communication strategies of [9] with the tensor partitioning strategy of [14] to employ secondary storage when quantum states are too large to fit in aggregate primary memory. Because secondary storage is typically orders of magnitude slower than main memory, the viability of using it depends on the extent to which the number of read/write cycles can be minimized or overlapped with computation. To this end, we first employ the in-memory methods of [14], aiming to maximize the number of gates that can be simulated using available aggregate memory; the resulting quantum state is calculated in slices and written to secondary storage. The partitioning methods discussed in [9] can then be applied to the remaining gates in the circuit, setting the number of “local” qubits according to the size of aggregate memory, rather than the memory sizes available on individual processing nodes. This increases the size of the resulting tensor slices, allowing the application of many more gates to the local quantum state before additional secondary-storage read/write cycles are needed. The resulting subcircuits can be further partitioned into sub-subcircuits using the methods of [9], to minimize internode communication in the overall calculations. We now provide details about these partitionings for the specific circuits studied in this paper.

Figs. 3 and 4 illustrate the first level of circuit partitioning for 36-cycle Sycamore ABCDCDAB circuits with 53 and 54 qubits, respectively. In this first phase, we use the in-memory methods of [14] to simulate the subcircuits 1 and 2 illustrated in these figures, performing tensor contraction deferral on the gates labeled “cd.” The outer-most qubits of the resulting tensors are used as “global” qubits, with the corresponding slices contracted in order to allow the simulation of subcircuit 3, slice by slice. Each resulting slice for subcircuit 3 is written to disk. Fig. 5 illustrates the “global” qubits that are sliced in this first phase of simulation. In the case of the 53-qubit circuit, qubits 0–3 and 49–52 are sliced in the simulation of subcircuit 3; for the 54-qubit circuit, qubits 0–4 and 50–53 are sliced.

In the second phase, qubits 23–30 are sliced for the 53-qubit circuit and qubits 23–31 are sliced for the 54-qubit circuit. In both cases, for each slice, the slice is read from disk, the gates in subcircuit 4 shown in Figs. 3 and 4 for the respective circuits are applied, and the slice is written back to disk.

This process is repeated for each subsequent subcircuit, with the choice of sliced qubits alternating between those used for subcircuit 3 and those used for subcircuit 4. Specifically, for subcircuits 5, 7 and 9, in the 53-qubit circuit we slice qubits 0–3 and 49–52, while in the 54-qubit circuit we slice qubits 0–4 and 50–53. For subcircuits 6 and 8, in the 53-qubit circuit we slice qubits 23–30, while in the 54-qubit circuit we slice qubits 23–31. As with subcircuit 4, slices are read from disk, processed, and then written back to disk.

To ensure that we efficiently transfer data to/from secondary storage, we organize the data on secondary storage as 2^{16} logical files for the 53-qubit circuit, and 2^{18} logical files for the 54-qubit circuit. In the case of the 53-qubit circuit, files are indexed by the values of qubits 0–3, 23–30, and 49–52; each logical file contains 2^{37} complex amplitudes corresponding to qubits 4–22 and 31–48. In the case of

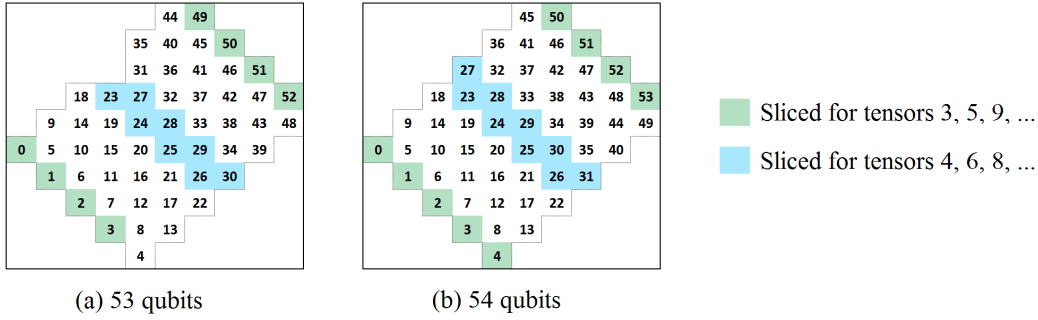


Figure 5: Qubit numbering scheme and first-level tensor slicing strategy for 53- and 54-qubit Sycamore circuits.

the 54-qubit circuit, files are indexed by the values of qubits 0–4, 23–31, and 50–53; each logical file contains 2^{36} complex amplitudes corresponding to qubits 5–22 and 32–49. Thus, in the first phase of simulation for the 53-qubit circuit (i.e., the phase in which tensor 3 is written to disk), we write 256 logical files to secondary storage for each of the 256 values of qubits 0–3 and 49–52 that are being sliced; these files correspond to the 256 possible values of qubits 23–30. For 54-qubit circuits, we write 512 logical files are written to secondary storage for each of the 512 values of qubits 0–4 and 50–53 that are being sliced; these files correspond to the 512 possible values of qubits 23–31.

In the second phase of simulation of the 53-qubit circuit (i.e., the phase in which subcircuit 4 is simulated), for each of the 256 values of qubits 23–30 that are being sliced, we read 256 logical files from secondary storage, corresponding to the 256 possible values of qubits 0–3 and 49–52. Once these 256 files of amplitudes are loaded into memory, we apply the gates in subcircuit 4 and write each updated slice back to storage. Similarly, for the 54-qubit circuit, for each of the 512 values of qubits 23–31 that are being sliced, we read 512 logical files from secondary storage, corresponding to the 512 possible values of qubits 0–4 and 50–53. Updated slices are written back to secondary storage as 512 files of amplitudes. These access patterns are repeated for each subsequent phase of processing. The above approach guarantees that individual logical files are never read or written redundantly, thereby minimizing access overhead per read/write cycle.

The above slicing strategy is designed to minimize the number of disk accesses by maximizing the number of “local” qubits employed in each disk slice, which is 45 qubits for both the 53- and the 54-qubit circuit. As discussed earlier, the slicing methodology in [9] is applied recursively to these 45-qubit slices, to minimize the number of all-to-all communication steps that must be performed in order to simulate subcircuits 3–9, shown in Figs. 3 and 4. Figs. 6–11 illustrate these recursive partitionings for tensors 3, 4, and 5 in the case of 20-cycle circuits. These partitionings correspond to slicing an additional 13 qubits (i.e., in addition to the qubits sliced for disk access purposes), in order to distribute work across 4096 nodes and across each pair of IBM Power 9 sockets within those nodes. We employ a socket-level slicing strategy to enable each socket to work independently, and to avoid Non-Uniform Memory Access (NUMA) overhead when memory accesses cross socket boundaries.

As shown in Figs. 6 and 9, subcircuit 3 is recursively partitioned into three sub-subcircuits labeled 3, 4, and 5. For the 53-qubit circuit, the sub-subcircuit labeled 3 is sliced on qubits 4–10 and 43–48, and for the 54-qubit circuits we slice qubits 5–10 and 43–49. These specific qubits are selected so that the corresponding slices of tensors 1 and 2, which are small, can be pre-distributed across sockets; this way, the contractions needed to start simulating subcircuit 3 can be performed in-place without communication. For 53-qubit circuits, the sub-subcircuit labeled 4 is sliced on qubits 4–16, and for 54-qubit circuits on qubits 5–17. This redistribution requires an all-to-all exchange of amplitudes across

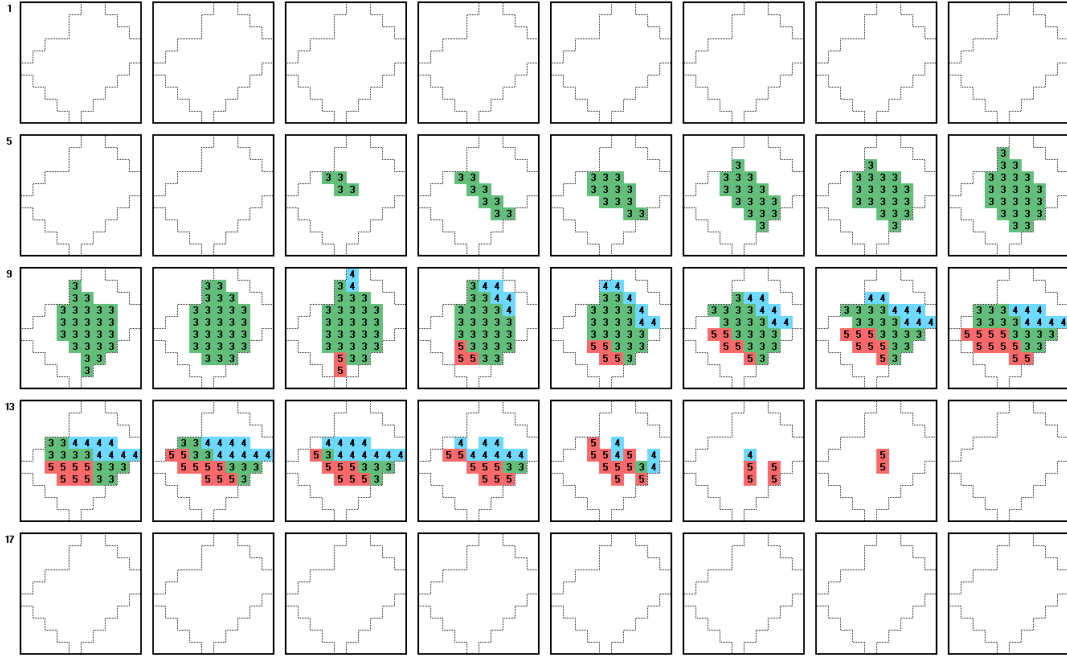


Figure 6: Partitioning of subcircuit 3 to minimize all-to-all communication for the 20-cycle, 53-qubit Sycamore circuit shown in Fig. 1.

sockets. For 53-qubit circuits, the sub-subcircuit labeled 5 is sliced on qubits 36–48, and for 54-qubit circuits on qubits 37–49, again requiring all-to-all communication.

As shown in Figs. 7 and 10, subcircuit 4 is recursively partitioned into two sub-subcircuits labeled 4 and 5. For 53-qubit circuits, the sub-subcircuit labeled 4 is sliced on qubits 40–52, and for 54-qubit circuits on qubits 41–53. The sub-subcircuit labeled 5 is sliced on qubits 0–12 for both 53- and 54-qubit circuits. Similarly, as shown in Figs. 8 and 11, subcircuit 5 is recursively partitioned into two sub-subcircuits labeled 5 and 6. For 53-qubit circuits, the sub-subcircuit labeled 5 is sliced on qubits 36–48, and for 54-qubit circuits on qubits 37–49. The sub-subcircuit labeled 6 is sliced on qubits 4–16 for 53-qubit circuits, and on qubits 5–17 for 54-qubit circuits.

5 Estimated running times

We estimate running times for the above simulation strategy on the Summit supercomputer using a combination of published performance figures, and internal IBM benchmarks performed as part of the installation process for Summit.

Because we directly employ the partitioning strategy of [9] in a recursive fashion, and because the resulting 45-qubit disk slices coincide with the 45-qubit circuits simulated in in [9], we use the performance figures in [9] to estimate per-disk-slice computational costs. This implicitly assumes that we are directly using the implementation described in [9] for the computations. Since [9] employs 8,192 nodes of the Cori II supercomputer, we can more easily extrapolate predicted performance across a corresponding 8,192 sockets on Summit.

To account for the differences between the gate set of [9] and Sycamore circuits, we use the following two facts: in [9], gates are aggregated together into k -qubit kernels represented by $2^k \times 2^k$ unitary matrices; and amplitudes are updated using matrix-vector calculations. The gate aggregation effectively normalizes computations across gate sets, making them independent from the details of individual gates.

Tensor	Disk transfers per disk slice	All-to-alls per disk slice	5Q kernels per disk slice	Tensor ranks per socket	Num gates	Contraction cost tot. FLOPs	Compute time (days)	% of total time	Achieved PFLOPS
1		0.000977	28	28	84	$1.181 \cdot 10^{21}$	0.002082	0.08%	0.0308
2		0.000977	25	27	84		0.001859	0.07%	0.0173
Contraction				31			0.117058	4.59%	116.7304
3.3			16	32	63		0.010658	0.42%	18.4865
3.4		1	6	32	23		0.003997	0.16%	17.9975
3.5		1	8	32	26		0.005329	0.21%	15.2587
Disk write	1	1							
Disk read	1	1							
4.4			11	32	49		0.007327	0.29%	20.9141
4.5		1	10	32	45		0.006661	0.26%	21.1275
Disk write	1	1							
Disk read	1	1							
5.5			9	32	35		0.005995	0.24%	18.2583
5.6		1	7	32	21		0.004663	0.18%	14.0850
Disk write	1	1							
Subtotals									
Compute			120			$1.181 \cdot 10^{21}$	0.165631	6.50%	87.4462
All-to-alls		9.001953					0.487725	19.13%	
Disk I/O	5						1.896296	74.37%	
Total	5	9.001953	120	32.67243	430		2.549652	100.00%	87.4462

Table 1: Running time estimates to simulate the 20-cycle, 53-qubit Sycamore circuit shown in Fig. 1. Tensors 3.3, 3.4, and 3.5 correspond to the partitionings of subcircuit 3 shown in Fig. 6, tensors 4.4 and 4.5 to the partitionings of subcircuit 4 shown in Fig. 7, and tensors 5.5 and 5.6 to the partitionings of subcircuit 5 shown in Fig. 8. The number of 5-qubit kernels is the number of aggregated gates spanning no more than 5 qubits, created by grouping gates together within each subcircuit. The contraction cost is the total number floating-point operations needed to perform the tensor contractions associated with entanglement indices, when tensors 1 and 2 are contracted in preparation for simulating subcircuit 3. The tensor ranks per socket indicate the sizes of the corresponding tensors in terms of the effective number of local qubits per socket. For entries above the subtotal line, the compute times are either the estimated times to perform gate operations based on the number of 5-qubit kernels, or the estimated time to perform the tensor 1 and 2 contractions, depending on the row in the table. Entries below the subtotal line factor in the costs of performing all-to-all communication and disk I/O. In the case of gate operations, the achieved PetaFLOPs per second column is the total number of floating-point operations without gate aggregation divided by the estimated compute time with gate aggregation.

Tensor	Disk transfers per disk slice	All-to-alls per disk slice	5Q kernels per disk slice	Tensor ranks per socket	Num gates	Contraction cost tot. FLOPs	Compute time (days)	% of total time	Achieved PFLOPS
1		0.001953	28	30	84	$9.445 \cdot 10^{21}$	0.004164	0.07%	0.0616
2		0.001953	26	30	87		0.003867	0.07%	0.0687
Contraction				33			0.936466	16.14%	116.7304
3.3			15	32	59		0.019984	0.42%	18.4865
3.4		1	8	32	31		0.010658	0.18%	18.1931
3.5		1	8	32	27		0.010658	0.18%	15.8456
Disk write	1	1							
Disk read	1	1							
4.4			11	32	49		0.014655	0.25%	20.9141
4.5		1	10	32	45		0.013323	0.23%	21.1275
Disk write	1	1							
Disk read	1	1							
5.5			9	32	37	0.011990	0.21%	19.3016	
5.6		1	7	32	21	0.009326	0.16%	14.0850	
Disk write	1	1							
Subtotals						$9.445 \cdot 10^{21}$			
Compute			122				1.035091	17.84%	107.2342
All-to-alls		9.003906					0.975661	16.81%	
Disk I/O	5						3.792593	65.35%	
Total	5	9.003906	122	33.80735	440		5.803345	100.00%	107.2342

Table 2: Running time estimates to simulate the 20-cycle, 54-qubit Sycamore circuit shown in Fig. 2. Tensors 3.3, 3.4, and 3.5 correspond to the partitionings of subcircuit 3 shown in Fig. 9, tensors 4.4 and 4.5 to the partitionings of subcircuit 4 shown in Fig. 10, and tensors 5.5 and 5.6 to the partitionings of subcircuit 5 shown in Fig. 11. The number of 5-qubit kernels is the number of aggregated gates spanning no more than 5 qubits, created by grouping gates together within each subcircuit. The contraction cost is the total number floating-point operations needed to perform the tensor contractions associated with entanglement indices, when tensors 1 and 2 are contracted in preparation for simulating subcircuit 3. The tensor ranks per socket indicate the sizes of the corresponding tensors in terms of the effective number of local qubits per socket. For entries above the subtotal line, the compute times are either the estimated times to perform gate operations based on the number of 5-qubit kernels, or the estimated time to perform the tensor 1 and 2 contractions, depending on the row in the table. Entries below the subtotal line factor in the costs of performing all-to-all communication and disk I/O. In the case of gate operations, the achieved PetaFLOPs per second column is the total number of floating-point operations without gate aggregation divided by the estimated compute time with gate aggregation.

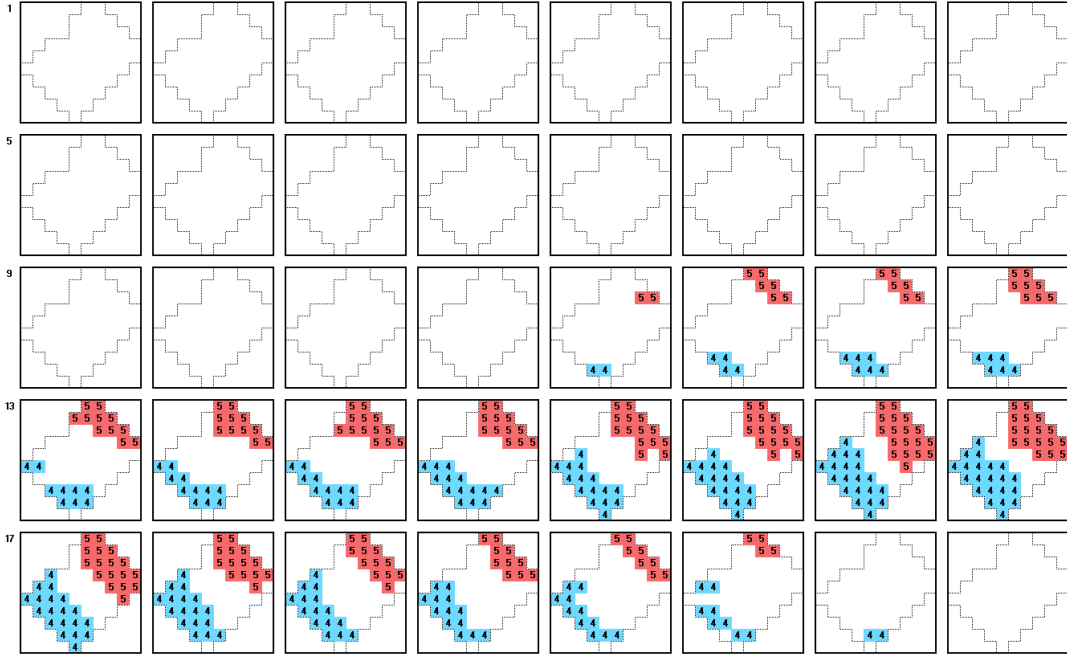


Figure 7: Partitioning of subcircuit 4 to minimize all-to-all communication for the 20-cycle, 53-qubit Sycamore circuit shown in Fig. 1.

For simulations performed on Cori II, gate aggregation in [9] uses $k_{max} = 5$, with actual kernel sizes sometimes being less than 5 qubits depending on the aggregated gates. To leverage the performance figures reported in [9], we therefore perform the same style of gate aggregation on Sycamore circuits. The tables shown in Tabs. 1 and 2 summarize the results obtained with these gate aggregations for the 53- and 54-qubit circuits illustrated in Figs. 1 and 2, respectively. In these tables, the “5-qubit kernels per disk slice” column identifies the number of aggregate gates constructed for each subcircuit and sub-subcircuit.

After gate aggregation, we estimate execution times for gate operations using Tables 1 and 2 in [9]. Specifically, we use the “Time” and “Comm.” columns of Table 2 in [9] to estimate computation time from total execution time, by factoring out the reported percentage of communication and synchronization time. We then divide the computation times by the number of aggregate gates (i.e., clusters) listed in Table 1 in [9] to obtain overall average execution times per aggregate gate. These averages can be used to estimate execution times for arbitrary numbers of aggregate gates, assuming simulations are performed on Cori II. To obtain corresponding time estimates for Summit, we scale the estimates by the ratio of the High Performance Linpack (HPL) benchmark figure for Cori II (14,014.70 PetaFLOPs/sec) versus Summit (148,600.00 PetaFLOPs/sec); this accounts for the significantly greater performance of Summit when performing, e.g., the matrix-vector calculations entailed by the use of gate aggregation. The calculations for 45-qubit simulations yield an expected execution time of 2.38380 seconds per aggregate gate on Cori II, and 0.22482 seconds per aggregated gate on Summit. The runtime estimates shown in Figs. 1 and 2 for tensors 3, 4 and 5 are obtained by multiplying the number of aggregate gates in each of their sub-subcircuits by 0.22482 seconds, and further multiplying by the number of disk slices per tensor (i.e., 256 slices for the 53-qubit circuit and 512 slices for the 54-qubit circuit). Tensors 1 and 2, on the other hand, represent 30-qubit calculations or less; therefore, we use the 30-qubit performance figures from Tables 1 and 2 in [9] to obtain an estimated 0.025097 seconds per aggregate gate on Summit for these tensors.

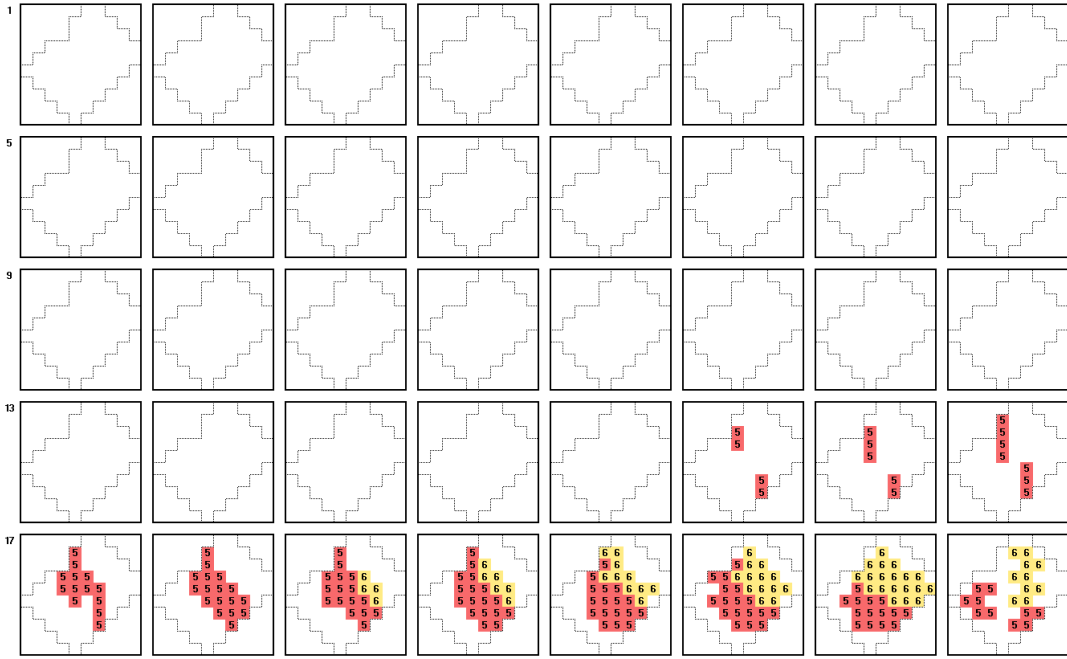


Figure 8: Partitioning of subcircuit 5 to minimize all-to-all communication for the 20-cycle, 53-qubit Sycamore circuit shown in Fig. 1.

The “achieved FLOPs per second” columns in Figs. 1 and 2 provide a sanity check for the above time estimates. For rows corresponding to gate operations, this column reports the number of floating-point operations that would be performed without gate aggregation divided by the estimated execution times. As such, the resulting figures provide an indication of the implied efficiency of the time estimates. As can be seen, the time estimates for gate operations are all near or below 11% of the 191 PetaFLOPs/sec peak double-precision performance expected across 8,192 sockets. Therefore, there is room to potentially improve upon these estimates by leveraging the SIMD capabilities of Summit’s NVIDIA GPUs: this would allow the simulation of individual gate operations, without resorting to gate aggregation, and the use of cuBLAS routines to implement the corresponding matrix-vector operations.

To obtain time estimates for the contractions of tensors 1 and 2, we use the performance figures reported in Table 1 in [17]. The simulation method presented in [16, 17] employs the “bristle-brush” strategy outlined in [13]. A key characteristic of this simulation strategy is that computations are dominated by very large tensor contractions across many tensor indices simultaneously. Consequently, we directly use the performance figures reported in Table 1 in [17] to estimate contraction times. Because we assume double-precision calculations, as in [9], we convert the performance figures in [17] from single-precision to double-precision. To do so, we multiply the single-precision computation rates of [17] by the ratio between the double-precision (7.8 TeraFLOPs/sec) and single-precision (15.7 TeraFLOPs/sec) peak performance rate of Summit’s NVIDIA GPUs. Performing this calculation and taking the worst case yields as estimated 14.249 TeraFLOPs per socket (116.73 PetaFLOPs/sec for 8,192 sockets). We use this rate in Figs. 1 and 2 to estimate execution times for the contraction of tensors 1 and 2.

We estimate all-to-all and disk I/O times using results from internal IBM benchmarks performed during the installation of Summit. These benchmarks indicate that a network injection rate of 7 GB/sec per node (3.5 GB/sec per socket) should be achievable during an all-to-all across the entire machine. This figure represents $\approx 30\%$ of the 23 GB/sec per node peak injection rate (11.5 GB/sec per socket) that characterizes the bisection bandwidth of Summit. The maximum reported file-system transfer rate

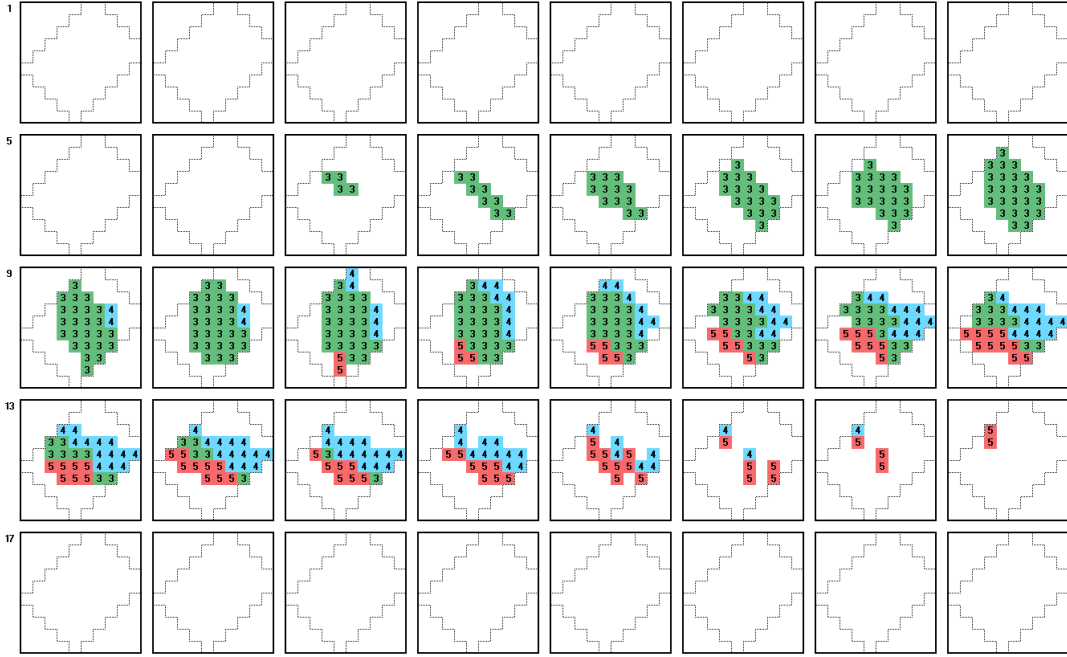


Figure 9: Partitioning of subcircuit 3 to minimize all-to-all communication for the 20-cycle, 54-qubit Sycamore circuit shown in Fig. 2.

is 2.2 TB/sec for random-access I/O (2.5 TB/sec for pure sequential I/O). We assume that all disk storage operations use single precision, while in-memory calculations use double precision. Thus, the estimates in Figs. 1 and 2 are based on a transfer rate of 2 TB/sec and a storage density of 8 bytes per amplitude (i.e., single-precision complex). Benchmark tests suggest that allocating only a subset of nodes to the task of performing disk I/O can be more efficient because it may avoid contention; those nodes then become the distribution points to the rest of the system when spreading computations across a majority of the nodes. Figs. 1 and 2 model this arrangement by incorporating an all-to-all communication cost for every disk read or write operation.

A summary of these estimates is plotted in Figs. 1 and 2. As these figures show, with the performance model discussed in this section we obtain an overall estimate of 2.55 days to compute all 2^{53} amplitudes of a 20-cycle, 53-qubit, Sycamore ABCDCDAB circuit with all amplitudes stored on disk, and 5.80 days for the corresponding 54-qubit circuit. To store amplitudes on disk in single precision, 64 PB of disk space are required for 53-qubit circuits, and 128 PB for 54-qubit circuits. Both fit within the 250 PB available on Summit.

The above analysis can be repeated for all depths suggested by Figs. 3 and 4; i.e., 10, 14, 20, 24, 28, 32, and 36 cycles. Doing so yields the results reported in Tables 3 and 4, and plotted in Fig. 12. As these tables and figure illustrate, estimated execution times grow linearly with the depth of the circuits. We remark that the required disk space remains constant, because with the above approach there is a maximum number of slices that are stored on disk at any given time. Thus, the disk occupation is 64 PB for 53-qubit circuits and 128 PB for 54-qubit circuits, regardless of the number of cycles.

References

- [1] S. Aaronson and L. Chen. Complexity-theoretic foundations of quantum supremacy experiments. *arXiv preprint arXiv:1612.05903*, 2016.

Number of Cycles	Disk Xfers per Disk Slice	All-to-Alls per Disk Slice	5-Qubit Kernels per Disk Slice	Run Time (days)
10	1	3.002	65	0.67
14	3	6.002	89	1.61
20	5	9.002	120	2.55
24	7	13.002	141	3.54
28	9	16.002	162	4.47
32	11	20.002	182	5.46
36	13	24.002	206	6.45

Table 3: Estimates of total run times for simulating 53-qubit, Sycamore ABCDCDAB circuits of various depths.

Number of Cycles	Disk Xfers per Disk Slice	All-to-Alls per Disk Slice	5-Qubit Kernels per Disk Slice	Run Time (days)
10	1	3.004	66	2.05
14	3	6.004	90	3.92
20	5	9.004	122	5.80
24	7	13.004	144	7.78
28	9	16.004	166	9.65
32	11	20.004	187	11.63
36	13	24.004	211	13.62

Table 4: Estimates of total run times for simulating 54-qubit, Sycamore ABCDCDAB circuits of various depths.

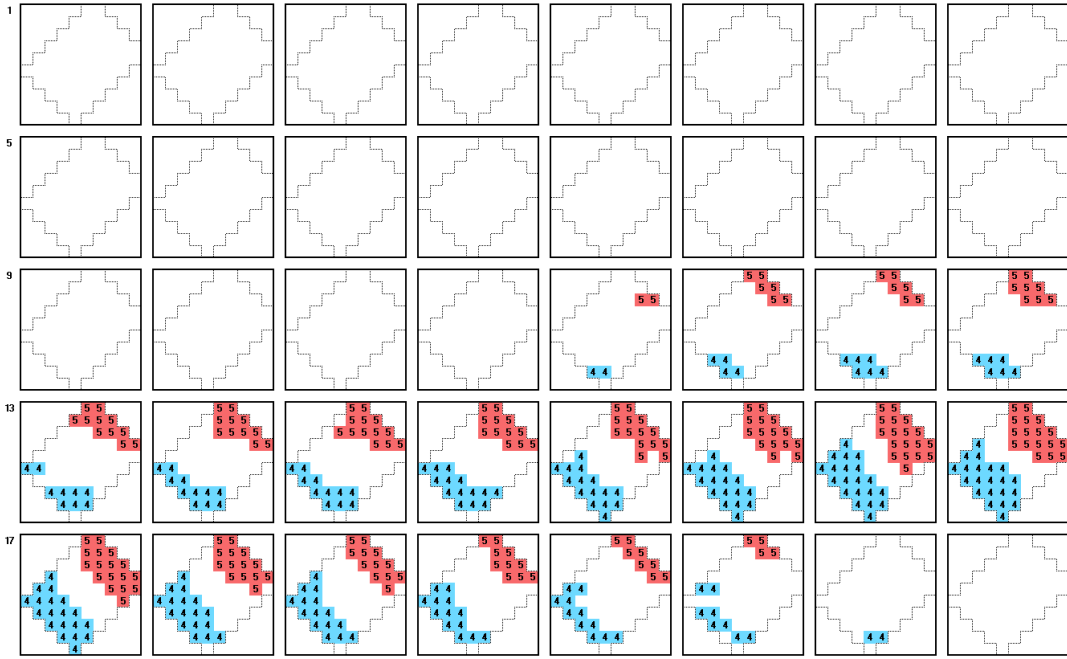


Figure 10: Partitioning of subcircuit 4 to minimize all-to-all communication for the 20-cycle, 54-qubit Sycamore circuit shown in Fig. 2.

- [2] S. Boixo, S. V. Isakov, V. N. Smelyanskiy, R. Babbush, N. Ding, Z. Jiang, M. J. Bremnen, J. M. Martinis, and H. Neven. Characterizing quantum supremacy in near-term devices. *Nature Physics*, 14(6):595–600, 2018.
- [3] S. Boixo, S. V. Isakov, V. N. Smelyanskiy, and H. Neven. Simulation of low-depth quantum circuits as complex undirected graphical models. *arXiv preprint arXiv:1712.05384*, 2017.
- [4] D. Castelvecchi. Quantum computers ready to leap out of the lab in 2017. *Nature*, 541:9–10, 2017.
- [5] J. Chen, F. Zhang, M. Chen, C. Huang, M. Newman, and Y. Shi. Classical simulation of intermediate-size quantum circuits. *arXiv preprint arXiv:1805.01450*, 2018.
- [6] M.-C. Chen, R. Li, L. Gan, X. Zhu, G. Yang, C.-Y. Lu, and J.-W. Pan. Quantum teleportation-inspired algorithm for sampling large random quantum circuits. *arXiv preprint arXiv:1901.05003*, 2019.
- [7] Z. Chen, Q. Zhou, C. Xue, X. Yang, G. Guo, and G. Guo. 64-qubit quantum circuit simulation. *arXiv preprint arXiv:1802.06952*, 2018.
- [8] C. Guo, Y. Liu, M. Xiong, S. Xue, X. Fu, A. Huang, X. Qiang, P. Xu, J. Liu, S. Zheng, H.-L. Huang, M. Deng, D. Poletti, W.-S. Bao, and J. Wu. General-purpose quantum circuit simulator with projected entangled-pair states and the quantum supremacy frontier. *arXiv preprint arXiv:1905.08394*, 2019.
- [9] T. Häner and D. S. Steiger. 0.5 petabyte simulation of a 45-qubit quantum circuit. In *Proceedings of the International Conference for High Performance Computing, Networking, Storage and Analysis, SC '17*, pages 33:1–33:10, New York, NY, USA, 2017. ACM.

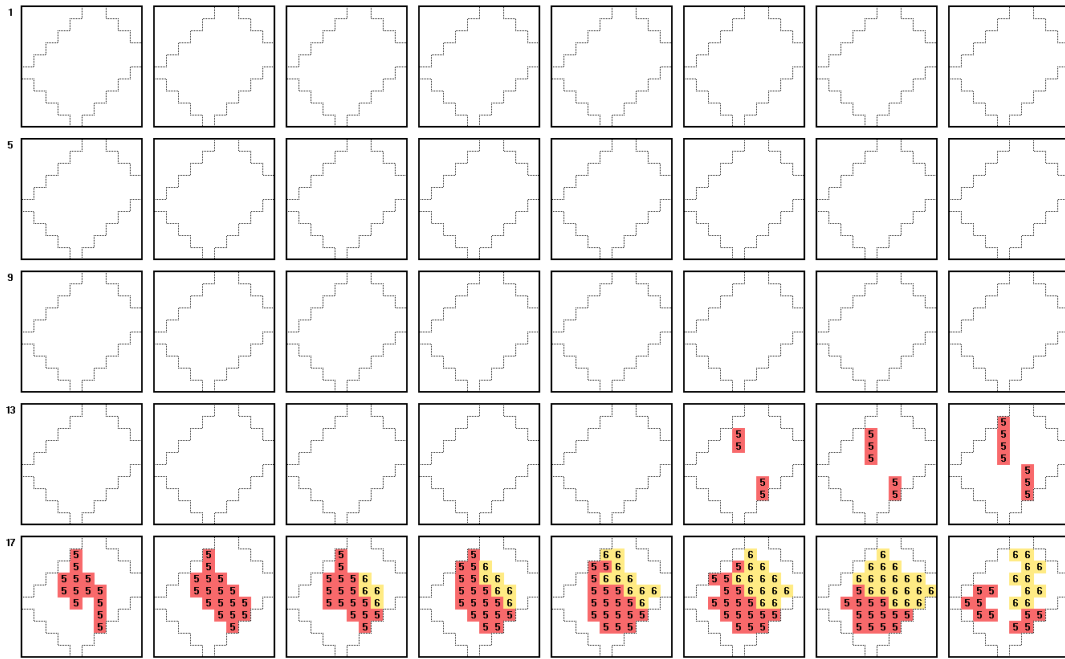


Figure 11: Partitioning of subcircuit 5 to minimize all-to-all communication for the 20-cycle, 54-qubit Sycamore circuit shown in Fig. 2.

- [10] R. Li, B. Wu, M. Ying, X. Sun, and G. Yang. Quantum supremacy circuit simulation on sunway taihulight. *arXiv preprint arXiv:1804.04797*, 2018.
- [11] I. L. Markov, A. Fatima, S. V. Isakov, and S. Boixo. Quantum supremacy is both closer and farther than it appears. *arXiv preprint arXiv:1807.10749*, 2018.
- [12] I. L. Markov and Y. Shi. Simulating quantum computation by contracting tensor networks. *SIAM Journal on Computing*, 38(3):963–981, 2008.
- [13] E. Pednault. Quantum computing—breaking through the 49 qubit simulation barrier. *IBM Research Blog posting also posted on phys.org* (<https://www.ibm.com/blogs/research/2017/10/quantum-computing-barrier/> and <https://phys.org/news/2017-10-quantum-computing-breaking-qubit-simulation-barrier.html>), 2017.
- [14] E. Pednault, J. A. Gunnels, G. Nannicini, L. Horesh, T. Magerlein, E. Solomonik, and R. Wisnieff. Breaking the 49-qubit barrier in the simulation of quantum circuits. *arXiv preprint arXiv:1710.05867*, 2017.
- [15] E. G. Rieffel and al. Quantum supremacy using a programmable superconducting processor. *NASA AMES Research Center Technical Report NASA/TP-2019-220319*, 2019.
- [16] B. Villalonga, S. Boixo, B. Nelson, C. Henze, E. Rieffel, R. Biswas, and S. Mandrà. A flexible high-performance simulator for the verification and benchmarking of quantum circuits implemented on real hardware. *arXiv preprint arXiv:1811.09599*, 2018.
- [17] B. Villalonga, D. Lyakh, S. Boixo, H. Neven, T. S. Humble, R. Biswas, E. G. Rieffel, A. Ho, and S. Mandrà. Establishing the quantum supremacy frontier with a 281 pflop/s simulation. *arXiv preprint arXiv:1905.00444*, 2019.

53- and 54-Qubit Sycamore Circuits with Single Precision Storage to Disk (8 bytes per amplitude)

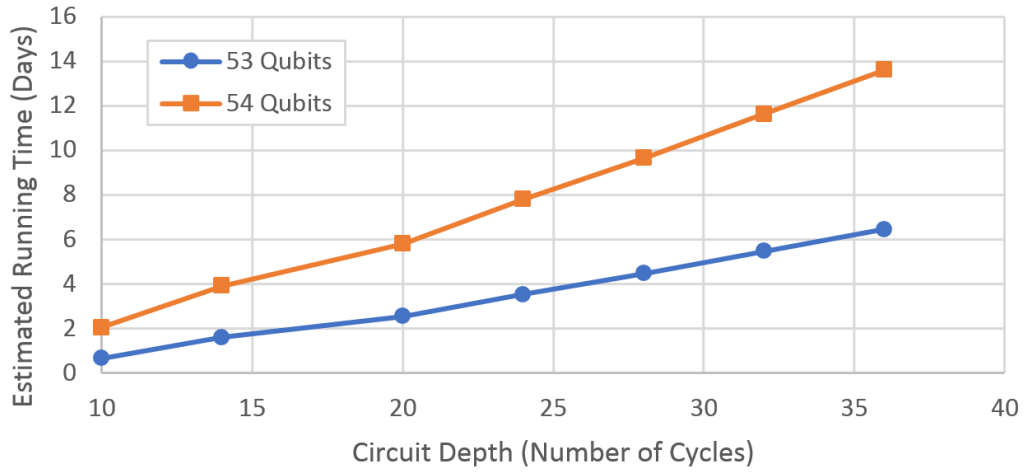


Figure 12: Graph of total runtime estimates for fully simulating both 53- and 54-qubit, Sycamore ABCD-CDAB circuits of various depths, with all amplitudes calculated and stored on disk.

- [18] F. Zhang, C. Huang, M. Newman, J. Cai, H. Yu, Z. Tian, B. Yuan, H. Xu, J. Wu, X. Gao, J. Chen, M. Szegedy, and Y. Shi. Alibaba cloud quantum development kit: Large-scale classical simulation of quantum circuits. *arXiv preprint arXiv:1907.11217*, 2019.